


Cite this: *RSC Adv.*, 2024, 14, 3845

# Post-treatment strategies for pyrophoric KOH-activated carbon nanofibres†

Tom Fischer,<sup>ab</sup> Ansgar Kretzschmar,<sup>a</sup> Victor Selmert,<sup>ab</sup> Sven Jovanovic,<sup>a</sup> Hans Kungl,<sup>a</sup> Hermann Tempel<sup>a</sup> and Rüdiger-A. Eichel<sup>ab</sup>

The effect of two atmospheric post-treatment conditions directly after the KOH activation of polyacrylonitrile-based nanofibres is studied in this work. As post-treatment different N<sub>2</sub>:O<sub>2</sub> flow conditions, namely high O<sub>2</sub>-flow and low O<sub>2</sub>-flow, are applied and their impact on occurring reactions and carbon nanofibres' properties is studied by thermogravimetric analysis (TGA), differential scanning calorimetry (DSC), scanning electron microscopy (SEM), Raman spectroscopy, elemental analysis and CO<sub>2</sub> and Ar gas adsorption. At high O<sub>2</sub>-flow conditions a pyrophoric effect was observed on the KOH-activated carbon nanofibers. Based on the obtained results from the TGA and DSC the pyrophoric effect is attributed to the oxidation reactions of metallic potassium formed during the KOH activation process and a consequent carbon combustion reaction. Suppression of this pyrophoric effect is achieved using the low O<sub>2</sub>-flow conditions due to a lower heat formation of the potassium oxidation and the absence of carbon combustion. Compared to the high O<sub>2</sub>-flow samples no partial destruction of the carbon nanofibers is observed in the SEM images. The determination of the adsorption isotherms, the surface area, the pore size distribution and the isosteric enthalpies of adsorption show the superior properties under low O<sub>2</sub>-flow conditions. The present micropore volume is increased from 0.424 cm<sup>3</sup> g<sup>-1</sup> at high O<sub>2</sub>-flow to 0.806 cm<sup>3</sup> g<sup>-1</sup> for low O<sub>2</sub>-flow samples, resulting in an increase of CO<sub>2</sub> adsorption capacity of 38% up to 6.6 mmol g<sup>-1</sup> at 1 bar. This significant improvement clearly points out the importance of considering highly exothermic potassium oxidation reactions and possible post-treatment strategies when applying KOH activation to electrospun carbon nanofiber materials.

Received 18th October 2023  
Accepted 30th December 2023

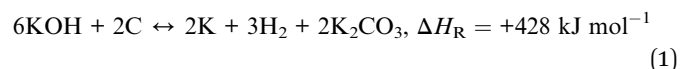
DOI: 10.1039/d3ra07096d

rsc.li/rsc-advances

## 1. Introduction

Carbon-based materials are widely applied in research and industry, *e.g.* as a component of devices for energy storage or as adsorbent in gas separation processes.<sup>1–6</sup> Amongst others, activated carbons are a frequently used material class due to their high micropore volume and high specific surface area. They are synthesized *via* a two-step process, comprised of carbonisation and activation. Typically, the precursor is first carbonised and subsequently activated, but also simultaneous carbonisation and activation processes are described.<sup>7–9</sup> The applied process and activation method depends on the desired surface morphology and porosity of the carbon for the individual application. Therefore, a variety of activation processes have been developed to optimise the pore structure of carbons, which can be divided into physical activation and chemical activation methods. Physical activation is done using oxidising

gases, *e.g.* CO<sub>2</sub> or H<sub>2</sub>O, whereas chemical activation uses solid activating agents, *e.g.* KOH or H<sub>3</sub>PO<sub>4</sub> to introduce porosity into the material.<sup>10–12</sup> As a chemical activating agent for carbon-based materials, KOH is well-established and was patented by Wennerberg *et al.* in 1978.<sup>13</sup> Since then, KOH activation has been widely used to activate many different precursor materials, *e.g.* coals, biomass and carbon fibres.<sup>11,12,14</sup> KOH is mainly applied to obtain a high micropore volume and a high specific surface area of the activated materials. Frequently reported BET areas for KOH activated carbon fibres range from 1000 up to 3000 m<sup>2</sup> g<sup>-1</sup> and the total pore volume easily reaches up to 2 cm<sup>3</sup> g<sup>-1</sup>.<sup>9,15</sup> Despite the widespread application for decades, the exact mechanism of the KOH activation is still discussed. As overall reaction for the KOH activation, eqn (1) is proposed.<sup>1,15–17</sup>



Nevertheless, the actual occurring reactions are a sequence of several parallel and consecutive reactions and highly depend on the used precursor.<sup>1,10,18–20</sup> The dehydration of KOH resulting in K<sub>2</sub>O and H<sub>2</sub>O (eqn (2)) is proposed as starting reaction for the KOH activation of petroleum coke.<sup>15,16</sup> On elevating the

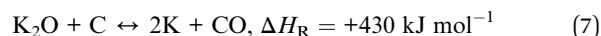
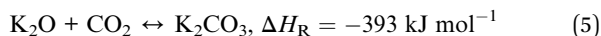
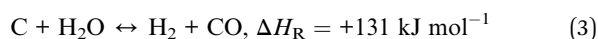
<sup>a</sup>Forschungszentrum Jülich GmbH, Institute of Energy and Climate Research (IEK-9) – Fundamental Electrochemistry, Jülich 52425, Germany

<sup>b</sup>RWTH Aachen University, Institute of Physical Chemistry, Aachen 52056, Germany

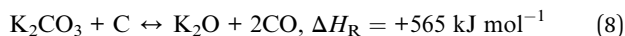
† Electronic supplementary information (ESI) available. See DOI: <https://doi.org/10.1039/d3ra07096d>



temperature, the carbon and the H<sub>2</sub>O are transformed into H<sub>2</sub> and CO *via* a coal gasification reaction (eqn (3)). Additional H<sub>2</sub>O reacts *via* the water gas shift reaction with the formed CO resulting in H<sub>2</sub> and CO<sub>2</sub> (eqn (4)). The obtained K<sub>2</sub>O (eqn (2)) and CO<sub>2</sub> (eqn (4)) are transformed to K<sub>2</sub>CO<sub>3</sub> at temperatures between 400 and 800 °C (eqn (5)). Furthermore, at reaction temperatures >700 °C K<sub>2</sub>O is reduced by H<sub>2</sub> and carbon to metallic potassium (eqn (6) and (7)), which can intercalate into the carbon lattice.<sup>16</sup>



Similar reactions were proposed for the KOH activation of multi-walled carbon nanotubes with the formation of K<sub>2</sub>CO<sub>3</sub> *via* redox reactions starting at 400 °C.<sup>17</sup> In subsequent reactions the K<sub>2</sub>CO<sub>3</sub> etches the carbon framework and K<sub>2</sub>O and CO are formed (eqn (8)).



Similar to the activation reactions on petroleum coke the formation of elemental potassium is described for temperatures higher than 700 °C (eqn (7)). Summarising the proposed reactions involved in KOH activation it can be agreed on three types of pore-forming reactions:

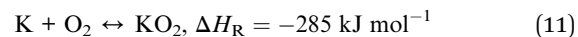
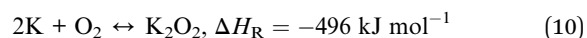
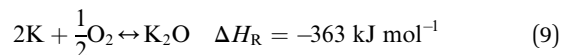
(a) Etching of the carbon material *via* redox reactions (eqn (3), (7), and (8))

(b) Pore formation through gasification, *i.e.* H<sub>2</sub>O, CO, CO<sub>2</sub>, H<sub>2</sub> (eqn (2)–(4), (6)–(8))

(c) Intercalation of elemental potassium (eqn (6) and (7)) into the carbon lattice, resulting in expansion of the carbon lattice.

Nevertheless, the actual reaction pathway highly depends on the applied activation parameters and the used precursor. Moreover, the structure of the precursor also affects the possibility of potassium intercalation. Overall, these impact factors render the assessment of the exact occurring reaction mechanisms a difficult task.<sup>1,20</sup>

Since the first patents, countless studies have been published on the impact of the different activation parameters, *e.g.* activation temperature, KOH:precursor ratio and activation duration.<sup>20,21</sup> In contrast, the impact of the atmospheric post-treatment conditions directly subsequent to KOH activation has not been investigated so far. However, this factor may have a serious impact on the obtained activated carbon due to the high reactivity of elemental potassium formed during KOH activation. Elemental potassium is known to react vigorously in the presence of oxygen and water due to the formation of potassium oxides according to eqn (9)–(11).<sup>22,23</sup>



The occurrence of such reactions in potassium-treated carbon materials has been frequently reported and was first observed by Fredenhagen and Cadenbach, who obtained pyrophoric potassium-graphite intercalation compounds in 1926.<sup>24,25</sup> Additionally, a similar pyrophoric effect is described for the intercalation products of coals and amorphous carbons with K<sub>2</sub>CO<sub>3</sub> during K<sub>2</sub>CO<sub>3</sub>-catalyzed gasification.<sup>26</sup> Such an intercalation of potassium from melts into graphite and carbons was detailed studied in several publications.<sup>25,27,28</sup>

The present work investigates, the occurrence of such a pyrophoric effect after KOH activation by application of two different atmospheric post-treatments. Therefore, electrospun PAN-based carbon nanofibres are used, which exhibited carbonisation temperature dependent molecular sieve properties and a remarkable CO<sub>2</sub>/N<sub>2</sub> adsorption selectivity in previous works.<sup>29–34</sup> TGA-MS, DSC, SEM, elemental analysis, Raman spectroscopy and gas adsorption techniques are used to investigate occurring reactions and changes to the fibre morphology and porosity.

## 2. Experimental

### 2.1 Carbon nanofibres synthesis

For the synthesis of the carbon nanofibres, solutions of 10 wt.% PAN (150 000 g mol<sup>−1</sup>, BOC Science, USA) in *N,N*-dimethyl formamide (VWR Chemicals, Germany) were prepared. All chemicals were used as received without further purification. To obtain a complete dissolution the mixtures were stirred for 48 h at room temperature. Subsequently, the solution was electrospun using an electrospinning device (IME Technologies, Netherlands). The polymer solution was supplied at a flow rate of 120 μL min<sup>−1</sup> through a 4-tip spinning needle. The spinneret was moved laterally to the collector drum with a speed of 20 mm s<sup>−1</sup> and a turn delay of 500 ms within a range of 120 mm. The spinning process was conducted at constant climate conditions of 25 °C and 30% relative humidity and the applied voltage was set to 25 kV. The tip-collector distance was 120 mm. The fibres were collected on a rotating drum with a diameter of 90 mm and a rotational speed of 1000 rpm. In total, the spinning was conducted for 3 h, which corresponds to 21.6 mL used spinning solution. Subsequently, oxidative stabilization at 250 °C in air for 15 h was performed at a heating rate of 5 K min<sup>−1</sup> using a drying cabinet (Binder GmbH, Germany). In the following step, 200 mg of the stabilized nanofibres were impregnated with 10 mL aqueous KOH (*c* = 0.26 mol L<sup>−1</sup>, KOH: PAN weight ratio 3:4) for 2 h. Afterwards, the sample was dried at 85 °C for 3 h to remove H<sub>2</sub>O.

The entire carbonisation & activation process was conducted inside a thermogravimetric analyser (STA 449 F1 Jupiter, Netzsch GmbH, Germany) coupled to a mass spectrometer



(QMS 403 D Aëlos, Netzsch GmbH, Germany) (TGA-MS). 200 mg of the obtained KOH impregnated nanofibres were transferred into the 5 mL TGA beaker to conduct the simultaneous carbonisation and activation. The TGA furnace was purged trifold with Ar to ensure an inert carbonisation atmosphere. Afterwards, the samples were heated at a rate of  $300\text{ K h}^{-1}$  up to  $800\text{ °C}$  and held for 3 h at this temperature in inert atmosphere at a flow rate of  $40\text{ mL min}^{-1}$  Ar 5.2 (Air Liquide, France). Afterwards, the samples were cooled down to  $40\text{ °C}$  at a rate of  $200\text{ K h}^{-1}$ . Once a temperature of  $40\text{ °C}$  was reached, the atmosphere was changed to an  $\text{O}_2:\text{N}_2$  atmosphere. The used  $\text{O}_2$ -flow rates were  $4\text{ mL min}^{-1}$  for low  $\text{O}_2$ -flow conditions and  $175\text{ mL min}^{-1}$  for high  $\text{O}_2$ -flow conditions. The respective  $\text{N}_2$  flow rates were  $16\text{ mL min}^{-1}$  for low  $\text{O}_2$ -flow conditions and  $75\text{ mL min}^{-1}$  for high  $\text{O}_2$ -flow conditions. After the switch to  $\text{O}_2:\text{N}_2$  atmosphere, the samples were kept for 45 minutes under the applied atmospheric conditions. After this process steps, the carbon nanofibres were obtained and neutralized using distilled water in several washing steps until a neutral pH value was achieved. Finally, the samples were dried at  $100\text{ °C}$ . For each post-treatment, a fivefold determination was carried out.

Additionally, similar experiments were conducted in a horizontal tube furnace (REST-E 400/6, Carbolite Gero GmbH & Co. KG, Germany). 200 mg of the KOH impregnated sample were transferred into an alumina boat and the furnace was trifold purged with Ar. Subsequently, the sample was heated up to  $800\text{ °C}$  at a heating rate of  $300\text{ K h}^{-1}$  in inert atmosphere at a flow rate of  $105\text{ L h}^{-1}$  Ar 5.2 (Air Liquide, France). The temperature was maintained for 3 h and afterwards cooled down at a rate of  $200\text{ K h}^{-1}$ . At a temperature of  $40\text{ °C}$  the furnace was opened and the samples were exposed directly to ambient air, which equals high  $\text{O}_2$ -flow conditions.

## 2.2 Material characterization

Mass and temperature changes, as well as the gaseous reaction products were detected by the TGA-MS system. The MS measurements were conducted in multiple ion detection (MID) mode. Relevant gases were identified with a scan measurement for  $m/z$  0–100 in an additional run prior to the actual measurements. The obtained MID runs were normalized to a reference run, to correct contamination of the device caused by the formation of soot particles during the reaction.

For data evaluation, the peak area for the detected components was determined by integration. The obtained weight normalized peak area is converted into the molar amount of  $\text{CO}_2$  based on a calibration using  $\text{CaC}_2\text{O}_4 \times \text{H}_2\text{O}$ . For the calibration masses of 50, 75, 100, 125 and 150 mg of  $\text{CaC}_2\text{O}_4 \times \text{H}_2\text{O}$  were transferred into the TGA crucible and afterwards heated to  $1000\text{ °C}$ . Based on the obtained results, a relation of peak area  $\text{CO}_2$  to molar amount could be drawn (S1).<sup>†</sup><sup>35</sup>

Additionally, differential scanning calorimetry (DSC) measurements were performed on a STA 449 F1 Jupiter (Netzsch GmbH, Germany) to measure the released reaction heats. Prior to the measurements, a calibration using a sapphire disc was performed. The DSC measurements were conducted with an equal heat treatment as for the carbonisation and activation

process in the TGA beaker. The sample mass of KOH impregnated nanofibres for these measurements was 20–30 mg. For each post-treatment condition, a triple determination was conducted.

Elemental analysis was conducted using a varioELcube elemental analyser (Elementar, Germany). A triple determination with 2 mg for each sample was carried out to determine C, H and N content. The O content was determined as the difference between the CHN content to the total composition.

Inductively coupled plasma optical emission spectroscopy (ICP-OES) was performed on iCAP 7600 analyser (ThermoFisher Scientific, USA). Two parallel digestions of 100 mg sample each were prepared in a furnace with 250 mg lithium borate. The samples were heated to  $1050\text{ °C}$  during 3 hours and maintained for 30 minutes at this temperature. The obtained melt was diluted in 50 mL 5%  $\text{HNO}_3$  and filled up to 100 mL.

A Quanta FEG 650 microscope (FEI, USA) was used to conduct the scanning electron microscopy (SEM) investigations. For image recording an acceleration voltage of 20 kV and an Everhart–Thornley detector was used. Small parts of the sample were fixed on the sample holders using copper strips.

Gas adsorption measurements were performed on a 3P micro 300 (3P Instruments, Germany). Argon (5.2, Air Liquide, France) adsorption measurements were conducted at 87 K and  $\text{CO}_2$  (4.5, Air Liquide, France) adsorption measurements at 273 K. Prior to the measurements the samples were outgassed at  $150\text{ °C}$  for 12 h.

The obtained data was evaluated using Asiqwin 5.0 (Quantachrome Instruments, USA). The adsorption isotherms were fitted as a Tóth isotherm<sup>36</sup> to calculate a mean isotherm for each parameter set. As error assessment the standard deviation was determined. A quenched solid state DFT (QSDFT) equilibrium model was applied to calculate the pore size distribution of the Argon adsorption data using a slit pore model on carbon. The pore size distribution of the  $\text{CO}_2$  adsorption isotherms was obtained by a Monte-Carlo model on carbon for slit pores.

Similar to the isotherm fits a mean value was calculated and the error indicated by the standard deviation. Additionally, the determination of the BET area, taking into account its limitations for microporous materials, was performed.<sup>37,38</sup>

Determination of the adsorption kinetics was performed using an Autosorb iQ 2 (Quantachrome, USA) by measurement of a single point isotherm at 50 mbar at 298 K using the VectorDose™ mode.

For calculation of the isosteric enthalpy of adsorption,  $\text{CO}_2$  adsorption isotherms were measured at 273 K, 283 K and 293 K on a QuadraSorb EVO (Quantachrome, USA) and fitted using a Tóth Fit. The calculation of the isosteric enthalpies of adsorption was conducted *via* the Clausius–Clapeyron approach.<sup>39</sup>

## 3. Results and discussion

In preliminary experiments KOH-activated carbon nanofibers were post-treated at ambient air as it is the usual procedure.<sup>1,11,12</sup> During the exposure to ambient air, a strong red glowing of the carbon nanofibres was observed, which indicates



Fig. 1 Pyrophoric KOH-activated electrospun PAN-based carbon nanofibres during exposure to ambient air directly after the simultaneous carbonisation and KOH activation. A red glowing of the carbon nanofibres can be observed (a Video of the glowing is attached as ESI†).

vigorous potassium oxidation reactions (Fig. 1 and Video in the ESI†).

Detailed investigations on this pyrophoric effect using a TGA-MS following the heat treatment in Fig. 2 were conducted to get a deeper insight into the occurring reactions. Therefore, two different post-treatment conditions were applied subsequent to the simultaneous carbonisation and activation: one, labelled as 'low O<sub>2</sub>-flow' at an O<sub>2</sub>-flow rate of 4 mL min<sup>-1</sup> (N<sub>2</sub>:O<sub>2</sub> 80:20) and a second one at 175 mL min<sup>-1</sup> (N<sub>2</sub>:O<sub>2</sub> 30:70), denoted as 'high O<sub>2</sub>-flow'. Additionally, SEM, DSC, elemental analysis, Raman spectroscopy and gas adsorption were used to obtain detailed information on the observed glowing, the reaction process and its impact on the fibre morphology.

### 3.1 High O<sub>2</sub>-flow

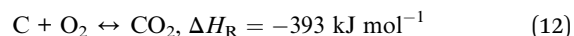
In Fig. 3a the mass and temperature changes of the freshly activated samples on switching the atmosphere from Ar to a mixture of N<sub>2</sub>:O<sub>2</sub> (30:70) are shown for the high O<sub>2</sub>-flow. The vertical dashed line indicates the switch from Argon to N<sub>2</sub>:O<sub>2</sub> (30:70) atmosphere at 175 mL min<sup>-1</sup> O<sub>2</sub>-flow. Almost instantly after the change in atmosphere, a mass gain of 2.8 ± 0.7 wt.% is observed. Afterwards, a mass loss of 3.1 ± 1.1% occurs before the mass slightly increases again. Simultaneously, the temperature rises to 130 °C and cools down again to the temperature

set point of 40 °C afterwards. However, it must be emphasized, that this is only an apparent temperature, as the reaction heat is partially consumed by the heat capacity of comparatively large TGA crucible. The actual temperature of the sample during the reaction is significantly higher.

The mass gain and the temperature rise can be assigned to the oxidation reactions of elemental potassium, which was formed during the KOH activation reactions (eqn (6) and (7)).<sup>22,23,40</sup> The formation of K<sub>2</sub>O (eqn (9)), K<sub>2</sub>O<sub>2</sub> (eqn (10)) and KO<sub>2</sub> (eqn (11)) releases high reaction enthalpies. The oxidation reactions most probably result in the formation of KO<sub>2</sub> for conditions with high availability of oxygen, due to the higher lattice stability compared to K<sub>2</sub>O and K<sub>2</sub>O<sub>2</sub>.<sup>22,23</sup>

The mass gain of 2.8 ± 0.7 wt.% corresponds to the O<sub>2</sub> uptake of 0.87 mmol g<sup>-1</sup>, which would require a potassium amount of 0.87 mmol g<sup>-1</sup> according to eqn (11). This corresponds to 14% of the total potassium, present at the carbon nanofibre samples, which was determined *via* ICP-OES (S2).† The calculated reaction heat of the formation of 0.87 mmol g<sup>-1</sup> KO<sub>2</sub> is -248 J g<sup>-1</sup> according to eqn (11), which is sufficient to cause a significant temperature rise.

However, these reactions cannot explain the subsequent mass loss of 3.1 ± 1.1 wt.%. An analysis of the gaseous products determined CO<sub>2</sub> as main emission (S3),† suggesting a carbon partial combustion reaction caused by the reaction heat of the potassium oxidation. A total carbon loss of 2.62 mmol g<sup>-1</sup> is calculated *via* eqn (12) accompanied by -1020 J g<sup>-1</sup> reaction heat. In total potassium oxidation and carbon combustion reactions result in an emitted reaction heat of -1268 J g<sup>-1</sup>.



Comparing the calculated reaction heats of KO<sub>2</sub> and CO<sub>2</sub> formation, the emitted reaction heat is caused to almost 80% by the carbon combustion to CO<sub>2</sub>. According to the basic heat equation of thermodynamics, the emitted heat could cause a temperature increase to a temperature higher than 700 °C, which would explain the observed glowing of the carbon nanofibres (Fig. 1).

Based on the calculated carbon loss the theoretical released amount of CO<sub>2</sub> would be 2.58 mmol g<sup>-1</sup>, which equals a CO<sub>2</sub>

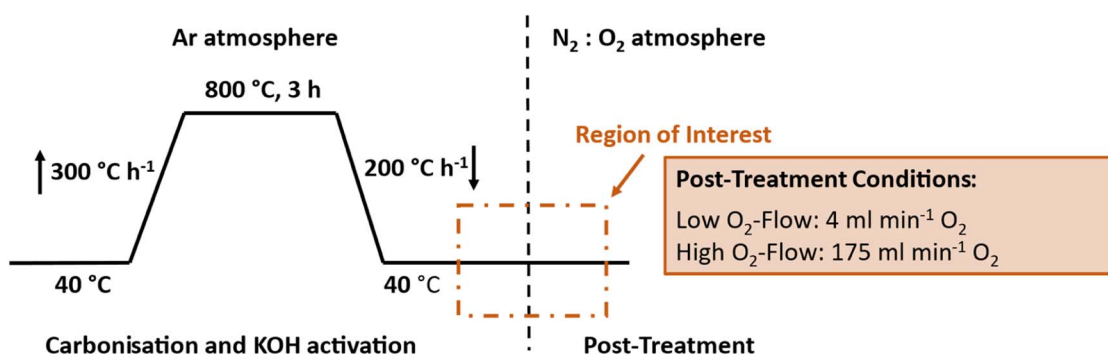
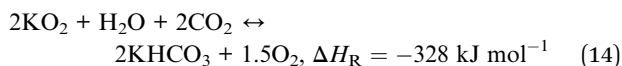
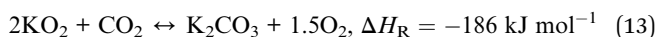


Fig. 2 Temperature profile of the applied simultaneous carbonisation and activation in Ar with subsequent post-treatment at 4 mL min<sup>-1</sup> (low O<sub>2</sub>-flow) and 175 mL min<sup>-1</sup> O<sub>2</sub>-flow (high O<sub>2</sub>-flow). The vertical dashed line indicates the switch from Ar to N<sub>2</sub>:O<sub>2</sub> atmosphere.





release of  $114 \text{ mg g}^{-1}$ . The amount of  $\text{CO}_2$  determined *via* quantification of the gaseous products is lower, giving a value of  $40.5 \text{ mg g}^{-1}$ . The significant difference could be explained by the emission of solid particles due to the vigorous reaction, which are not detected by the MS. Additionally, side reactions due to formed  $\text{KO}_2$  are possible during the reaction as listed in eqn (13) and (14). The possible side reactions mainly result in the formation of potassium carbonate and bicarbonate.<sup>41,42</sup>



Furthermore, combined TG-DSC measurements were conducted to obtain experimental data on the emitted reaction heats for high  $\text{O}_2$ -flow (Fig. 3b). The simultaneous TG measurement was done to assess the comparability of both measurements since different sized crucibles had to be used for both measurements. An emitted reaction heat of  $-2717 \text{ J g}^{-1}$  was determined for the post-treatment step at high  $\text{O}_2$ -flow (Fig. 3b). This value is about twice as high as the calculated reaction heat of  $-1268 \text{ J g}^{-1}$  from previous TG measurements (Fig. 3a).

The deviation of these two methods is explicable, when considering the shape of the TG signal of the DSC measurement. Similar to the first discussed TG signal, a mass gain is observed directly after the switch to the high  $\text{O}_2$ -flow. Subsequently, a significant mass loss due to carbon combustion occurs. However, the mass loss during the DSC measurement is  $8.2 \text{ wt.}\%$ , which is more than double the value of  $3.1 \text{ wt.}\%$  during the TG measurement. Due to the increased carbon combustion during the DSC measurement the obtained experimental value and the calculated reaction enthalpy from the TG measurement may not be directly comparable. The increased carbon combustion is probably caused by denser packed carbon nanofibres in the smaller DSC crucible, resulting in a stronger heat accumulation. This is an important hint, as the extent of potassium oxidation and carbon combustion reactions depend on the packing density and, therefore, heat and oxygen transport properties of the material.

Interestingly, similar observations are not described for KOH activation of commonly used carbon precursors, *e.g.* PAN powder,<sup>43,44</sup> carbon fibres,<sup>45–47</sup> biomass<sup>48–50</sup> and coals.<sup>18,51,52</sup> Although, the occurrence of these potassium oxidation reactions could be expected based on the proposed mechanisms for KOH activation mentioned in eqn (6) and (7). Therefore, PAN powder was used as reference material and activated using the identical conditions as for activation of the nanofibre material. During high  $\text{O}_2$ -flow post-treatment no pyrophoric effect was observed (S4).† Hence, the described pyrophoric effect is probably linked to the material structure induced by the electrospinning process and, possibly, the activation conditions.

Overall, the post-treatment at high  $\text{O}_2$ -flow conditions results in the uncontrolled oxidation of metallic potassium to  $\text{KO}_2$  causing a carbon combustion under severe formation of heat and a strong glowing of the carbon nanofibres.

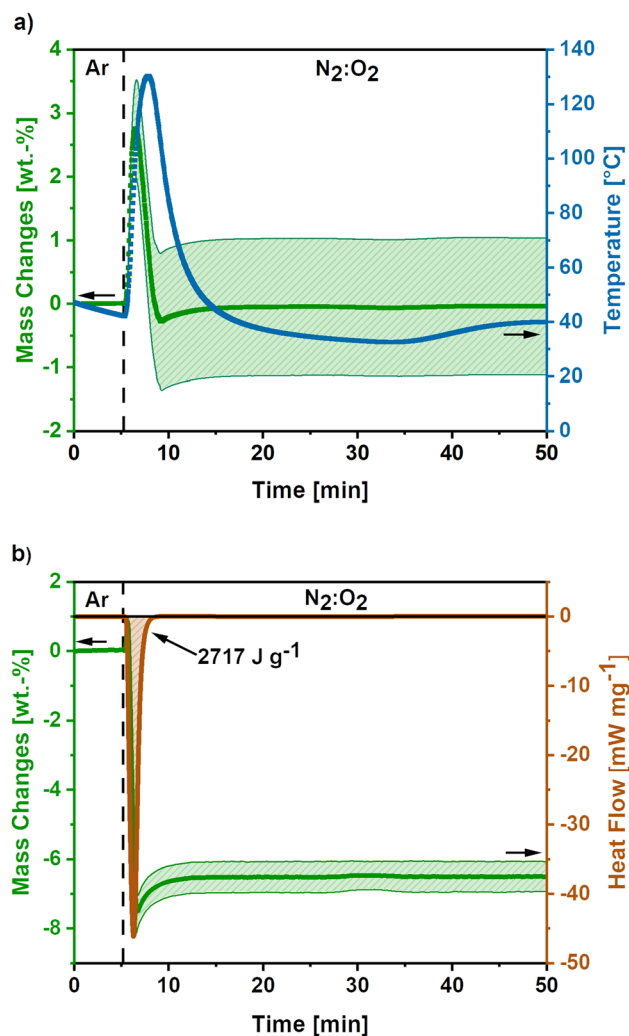


Fig. 3 (a) Mass and temperature changes during post-treatment at high  $\text{O}_2$ -flow conditions ( $175 \text{ mL min}^{-1} \text{ O}_2$ ). Average value of 5 measurements. The shaded areas show the standard deviation for the mass signal and the dashed line indicates the switch from Ar to  $\text{N}_2 : \text{O}_2$  atmosphere. (b) DSC-TGA data during high  $\text{O}_2$ -flow post-treatment of KOH-activated carbon nanofibres ( $\text{O}_2$ -flow  $175 \text{ mL min}^{-1}$ ), where the dashed line indicates the atmosphere switch. A release of  $-2717 \text{ J g}^{-1}$  reaction heat accompanied by a mass loss  $8.2 \text{ wt.}\%$  is observed.

### 3.2 Low $\text{O}_2$ -flow

To develop a treatment strategy to suppress the sample glowing, similar experiments were conducted using an  $\text{O}_2$ -flow of  $4 \text{ mL min}^{-1}$ , 'low  $\text{O}_2$ -flow'. Fig. 4a shows the mass and temperature changes after the switch of atmosphere from Ar to a mixture of  $\text{N}_2 : \text{O}_2$  ( $80 : 20$ ) with an  $\text{O}_2$ -flow rate of  $4 \text{ mL min}^{-1}$ , indicated by the dashed line.

A mass gain of  $1.5 \pm 0.1 \text{ wt.}\%$  accompanied by a minor temperature rise to  $45^\circ\text{C}$  after 8 minutes is observed after the atmosphere switch. Contrary to the high  $\text{O}_2$ -flow, no weight loss is observed. The mass gain can be explained by the uptake of  $\text{O}_2$  due to the oxidation of metallic potassium according to eqn (9)–(11). As the temperature increase is insufficient to cause a carbon combustion, no mass loss is observed.



The obtained mass gain equals an  $\text{O}_2$  uptake of  $0.44 \text{ mmol g}^{-1}$ , based on eqn (12) this results in the emission of  $-128 \text{ J g}^{-1}$  reaction heat. This calculated reaction heat is comparable to the experimental value of  $-94 \text{ J g}^{-1}$  obtained from additional DSC measurements (Fig. 4b) and causes a slight temperature rise on the carbon nanofibres. The slight deviation of the obtained reaction heats can be explained by the simple nature of the calculations used, which only considered one potassium formation reaction neglecting possible side reactions to the formation of other potassium oxide species.<sup>22,23,41</sup>

Summarising, the low  $\text{O}_2$ -flow post-treatment results in the controlled oxidation reactions during exposure to oxygen. The emitted reaction heat of  $-94 \text{ J g}^{-1}$  is significantly reduced compared to  $-2717 \text{ J g}^{-1}$  for high  $\text{O}_2$ -flow. Therefore, no indication for a carbon combustion or glowing was found.

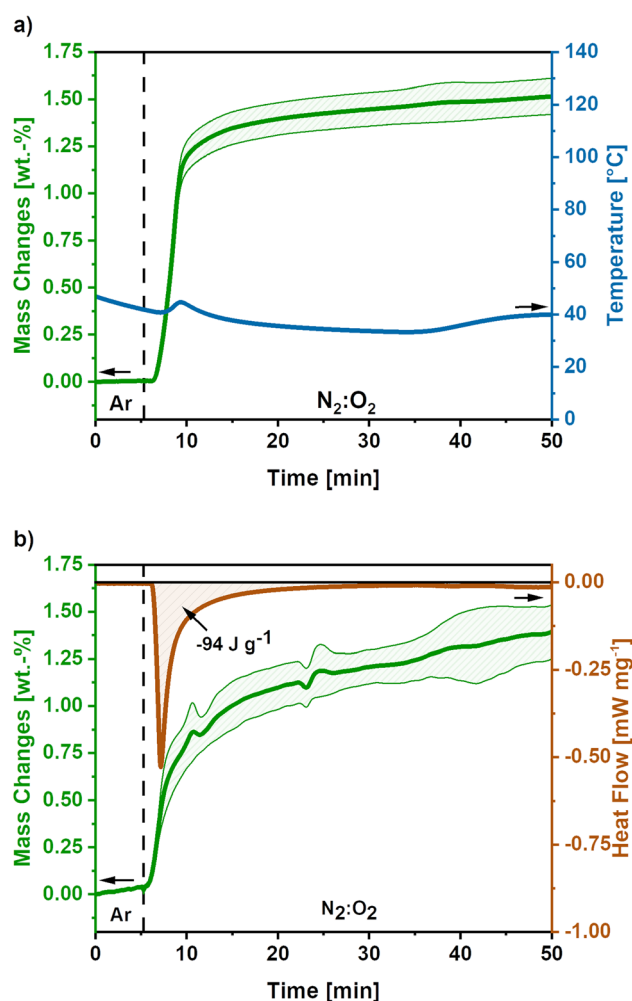


Fig. 4 (a) Mass and temperature changes after the switch to low  $\text{O}_2$ -flow ( $4 \text{ mL min}^{-1}$ ) obtained as mean value of 5 measurements. The dashed line indicates the switch from Ar to  $\text{N}_2:\text{O}_2$  atmosphere and the shaded areas show the standard deviation for the mass signal. (b) DSC-TGA signal for low  $\text{O}_2$ -flow post-treatment of activated carbon nanofibres based on 3 measurements. The dashed line indicates the switch to  $\text{N}_2:\text{O}_2$  atmosphere and the shaded areas show the standard deviation. After the switch a mass gain of  $1.5 \text{ wt.}\%$  is observed accompanied by an emitted reaction heat of  $-94 \text{ J g}^{-1}$ .

### 3.3 Comparison of high $\text{O}_2$ -flow and low $\text{O}_2$ -flow

Besides the previously discussed mass and temperature changes during the sample treatment with high  $\text{O}_2$ -flow and low  $\text{O}_2$ -flow, this section addresses differences in the emitted  $\text{CO}_2$  amount, elemental composition and morphological changes observed in SEM.

**3.3.1 Mass balances.** Fig. 5 shows the emitted amount of  $\text{CO}_2$  in  $\text{mmol g}^{-1}$  for high  $\text{O}_2$ -flow and low  $\text{O}_2$ -flow as measured by the MS. The detected  $\text{CO}_2$  amount for high  $\text{O}_2$ -flow is at  $1000 \mu\text{mol g}^{-1}$ , whereas the  $\text{CO}_2$  emission for low  $\text{O}_2$ -flow was at  $0.6 \mu\text{mol g}^{-1}$ . This means a reduction of the emitted  $\text{CO}_2$  amount of more than three orders of magnitude for low  $\text{O}_2$ -flow conditions. These results match with the absence of a mass loss for low  $\text{O}_2$ -flow discussed in the previous section.

Additionally, CHNO elemental analysis was conducted to detect changes in the elemental composition of the obtained carbon nanofibres for high and low  $\text{O}_2$ -flow (Table 1). The C content for low  $\text{O}_2$ -flow is  $69.6 \text{ wt.}\%$ , whereas it is at  $59.8 \text{ wt.}\%$  for high  $\text{O}_2$ -flow. This  $10 \text{ wt.}\%$  decreased C content can be related to the carbon combustion and possibly also to oxidation of the carbon surface. For the H and N content no significant changes were obtained between high  $\text{O}_2$ -flow and low  $\text{O}_2$ -flow. Regarding the O content, an increase of  $7 \text{ wt.}\%$  for high  $\text{O}_2$ -flow compared to low  $\text{O}_2$ -flow is observed. This is explained by the reduced amount of C relative to the O content and a partial oxidation of the carbon surface. However, the oxidation of the carbon surface would counteract the observed weight loss during the carbon combustion.

For further structural characterization and comparison, Raman spectroscopy was performed on low and high  $\text{O}_2$  flow samples. The results are shown and discussed in the ESI (S5).†

**3.3.2 Electron microscopy.** As the described glowing and combustion effect on high  $\text{O}_2$ -flow might cause severe changes to the surface morphology of the carbon nanofibres, high  $\text{O}_2$ -flow and low  $\text{O}_2$ -flow samples were investigated with SEM

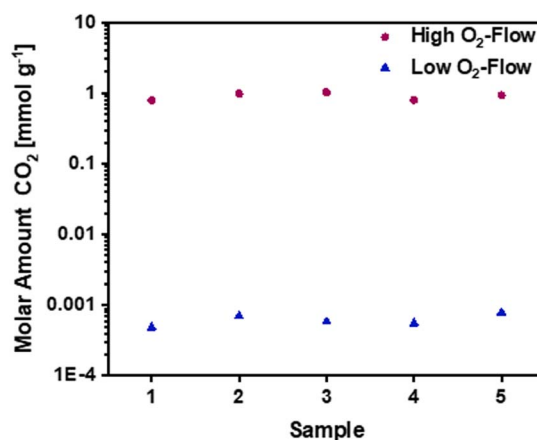


Fig. 5 Molar amounts of  $\text{CO}_2$  for high  $\text{O}_2$ -flow and low  $\text{O}_2$ -flow samples during post-treatment. Data obtained from MS measurements using a  $\text{CaC}_2\text{O}_4 \times \text{H}_2\text{O}$  calibration. A  $\text{CO}_2$  amount of  $1 \text{ mmol g}^{-1}$  for high  $\text{O}_2$ -flow compared to  $0.6 \mu\text{mol g}^{-1}$  for low  $\text{O}_2$ -flow was detected.



**Table 1** CHNO elemental composition for neutralized high O<sub>2</sub>-flow, low O<sub>2</sub>-flow and pristine carbon nanofibres. O content is calculated as difference for high O<sub>2</sub>-flow and low O<sub>2</sub>-flow. Elemental composition of the pristine carbon nanofibres taken from.<sup>30</sup> The value is the average of 5 measurements, the standard deviation is given as error

Sample	Elemental composition (wt%)			
	C	H	N	O
High O <sub>2</sub> -flow	59.8 ± 1	2.2 ± 0.4	12.7 ± 0.5	25.3 ± 3.1
Low O <sub>2</sub> -flow	69.6 ± 0.9	1.7 ± 0.2	10.7 ± 0.6	18.0 ± 2.8
Pristine fibres	72.6 ± 0.1	1.4 ± 0.1	16.2 ± 0.2	9.8 ± 0.7

(Fig. 6). For reference purposes the pristine fibres<sup>30</sup> are shown in Fig. 6a as well.

The pristine carbon nanofibres are randomly aligned and large void volumes are visible between the fibres. For the KOH activated carbon nanofibres smaller void volumes and fragmented fibres are observed. The low O<sub>2</sub>-flow samples exhibit a similar morphology as the pristine material (Fig. 6b, S6† vs. 6a). In contrast, high O<sub>2</sub>-flow samples (Fig. 6d) exhibit areas with significant destruction of surface morphology compared to the pristine material (Fig. 6a). The formation of voids in the size of up to 3 microns is clearly visible in the SEM images (Fig. 6d). These macropores are not homogeneously distributed on the surface of the high O<sub>2</sub>-flow samples as also areas with less severe destruction are visible (Fig. 6c). This observation could be explained by an inhomogeneous distribution of metallic potassium on the samples and, therefore, inhomogeneous severe heat formation due to the potassium oxidation reactions.

Summarising, the obtained SEM results prove that the control of post-treatment conditions significantly affects the

morphology of the samples. The applied O<sub>2</sub>-flow affects the potassium oxidation reactions and a severe destruction of the carbon nanofibres can be avoided by application of a low O<sub>2</sub>-flow as post-treatment.

**3.3.3 Gas adsorption properties.** To obtain detailed information on the impact of the different post-treatment conditions on the pore structure and the adsorption properties, gas adsorption measurements were conducted for high O<sub>2</sub>-flow and low O<sub>2</sub>-flow samples.

Argon adsorption measurements were performed at 87 K to assess the microporosity. The obtained adsorption isotherms exhibit a type I shape, which is typical for highly microporous adsorbents (Fig. 7a). In the low relative pressure range a steep increase is observed, which flattens for higher relative pressures and approaches a limiting value. The obtained isotherms exhibit similar shapes independent of post-treatment, although the obtained adsorption capacities are significantly higher on the low O<sub>2</sub>-flow samples. At 1 bar 17 mmol g<sup>-1</sup> CO<sub>2</sub> are adsorbed on the low O<sub>2</sub>-flow samples, whereas 31 mmol g<sup>-1</sup> CO<sub>2</sub> are obtained for high O<sub>2</sub>-flow. This equals an increase in adsorption capacity at 1 bar by 82%.

The pore size distribution was derived from the Ar adsorption isotherms using a density functional theory (DFT) kernel. The cumulative pore size distributions for low O<sub>2</sub>-flow and high O<sub>2</sub>-flow are shown in Fig. 7b. The comparison of the total pore volume  $V_{\text{DFT}(\text{tot})}$  and the pore volume of pores below 2 nm ( $V_{\text{DFT}<2\text{nm}}$ ) reveals that both samples have almost exclusively micropores (Table 2,  $V_{\text{DFT}<2\text{nm}}$ ). The obtained micropore volume is 0.806 cm<sup>3</sup> g<sup>-1</sup> for low O<sub>2</sub>-flow samples, which is an increase of 90% compared to 0.424 cm<sup>3</sup> g<sup>-1</sup> for the high O<sub>2</sub>-flow. Such values are comparable to values obtained by Im *et al.* and Chiang *et al.* for PAN-based activated carbon fibres.<sup>45,53</sup>

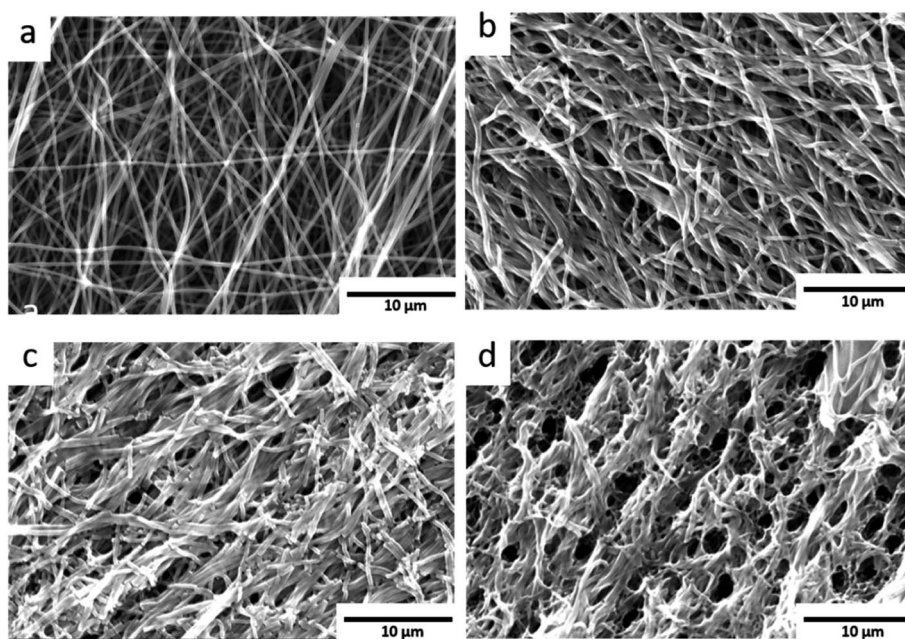


**Fig. 6** SEM images: (a) pristine carbon nanofibres shown as reference. (b) Low O<sub>2</sub>-flow samples without visible destruction of the fibre morphology. (c) High O<sub>2</sub>-flow samples with an area displaying a smaller degree of destruction (d) high O<sub>2</sub>-flow samples with severe destruction of the fibre morphology.



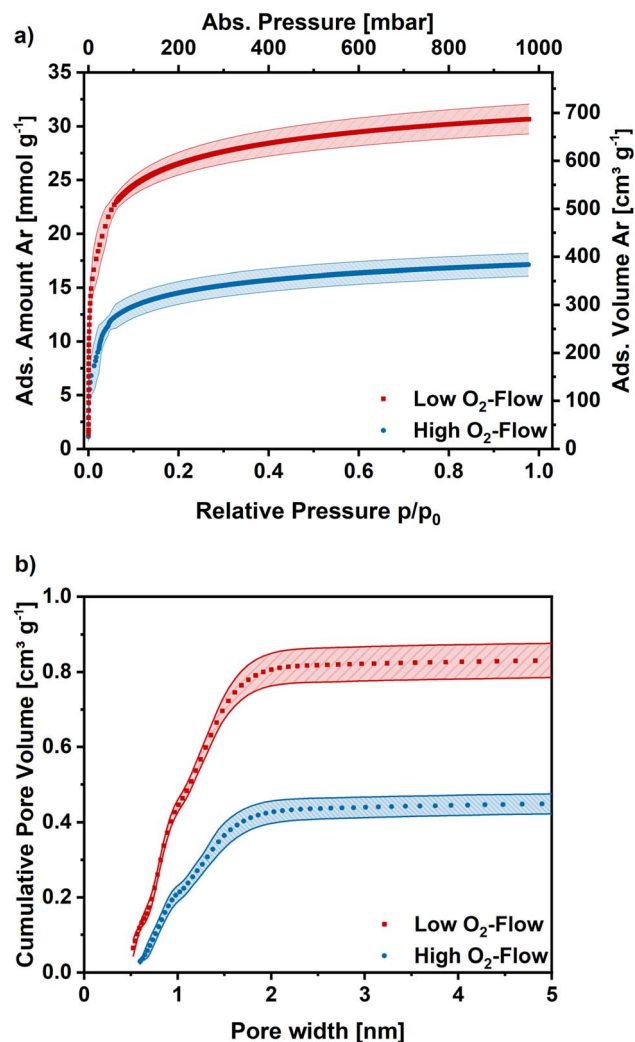


Fig. 7 (a) Ar adsorption isotherms obtained at 87 K for high O<sub>2</sub>-flow and low O<sub>2</sub>-flow. Average isotherm of 5 measurements. (b) Cumulative pore size distribution for high O<sub>2</sub>-flow and low O<sub>2</sub>-flow calculated with a DFT kernel. Shaded areas show the standard deviation.

The BET area was determined at 1094 m<sup>2</sup> g<sup>-1</sup> for high O<sub>2</sub>-flow and at 2029 m<sup>2</sup> g<sup>-1</sup> for low O<sub>2</sub>-flow, which are typical BET areas of KOH-activated carbons.<sup>9,44,54</sup> Especially the direct comparison to the BET area of the pristine fibres (13.4 m<sup>2</sup> g<sup>-1</sup>) clearly proves a successful KOH activation of the electrospun PAN-based carbon nanofibres. Additionally, the high impact of the applied post-treatment conditions on the surface morphology and porosity of the carbon nanofibres is obvious.

For more detailed micropore characterization CO<sub>2</sub> adsorption measurements at 273 K were performed. Fig. 8a shows the CO<sub>2</sub> adsorption isotherms for the pristine,<sup>30</sup> high O<sub>2</sub>-flow and the low O<sub>2</sub>-flow samples. The pristine fibres isotherm exhibits a high uptake at low relative pressures and turns more into a linear shape at higher relative pressures with a maximum CO<sub>2</sub> uptake of 2.7 mmol g<sup>-1</sup> at 1 bar. In comparison, the adsorption isotherm of the high O<sub>2</sub>-flow shows a lower CO<sub>2</sub> uptake at pressures below 200 mbar.

At pressures above 200 mbar the adsorption isotherm of CO<sub>2</sub> surpasses the adsorption isotherm of the pristine fibres and rises to 4.7 mmol g<sup>-1</sup> at 1 bar (Fig. 8). Contrary, the low O<sub>2</sub>-flow samples exhibit a similar uptake as the pristine fibres at low relative pressures and already surpasses the adsorption capacity of the pristine fibres at pressures of 75 mbar. At 1 bar it reaches an CO<sub>2</sub> adsorption capacity of 6.5 mmol g<sup>-1</sup>, which is 38% increase compared to the high O<sub>2</sub>-flow samples and even 140% increase compared to the pristine fibres.

In comparison to literature data the obtained CO<sub>2</sub> adsorption capacities are among the highest for KOH-activated electrospun carbon nanofibres. Wang *et al.* reported CO<sub>2</sub> adsorption capacities of 2.9 mmol g<sup>-1</sup> at 1 bar and 273 K, which is significantly lower than the reported values in the present work.<sup>47</sup> Comparable CO<sub>2</sub> adsorption capacities were reported by Chiang *et al.* and Zainab *et al.* who obtained 3.5 mmol g<sup>-1</sup> at 298 K, which is close to the obtained 4.2 mmol g<sup>-1</sup> at 293 K on the high O<sub>2</sub>-flow sample in this study (S6).<sup>† 55,56</sup>

The pore size distribution was determined using Monte-Carlo calculations and the cumulative pore volume is shown in Fig. 8b. As described previously for DFT calculations based on Ar adsorption, the pore volume increases for low O<sub>2</sub>-flow samples over the full range of pore sizes compared to the high O<sub>2</sub>-flow samples. The total pore volume is 0.61 cm<sup>3</sup> g<sup>-1</sup> for low O<sub>2</sub>-flow and 0.45 cm<sup>3</sup> g<sup>-1</sup> for high O<sub>2</sub>-flow samples, resulting in an increase in pore volume of 36% for the low O<sub>2</sub>-flow samples. Regarding the ultramicropore volume (<0.7 nm), high O<sub>2</sub>-flow samples exhibit a value of 0.15 cm<sup>3</sup> g<sup>-1</sup>, which is enhanced to 0.21 cm<sup>3</sup> g<sup>-1</sup> on low O<sub>2</sub>-flow samples. Overall, the obtained pore volumes from CO<sub>2</sub> adsorption isotherms are comparable to those obtained from Argon isotherms, except for a significant difference of the obtained micropore volume below 1.5 nm for DFT (0.365 cm<sup>3</sup> g<sup>-1</sup>) and Monte-Carlo (0.446 cm<sup>3</sup> g<sup>-1</sup>) data for high O<sub>2</sub>-flow. This deviation could be caused by the different surface chemistry of samples prepared at high and low O<sub>2</sub>-flow. High O<sub>2</sub>-flow samples exhibit a higher oxygen content than low O<sub>2</sub>-flow samples, which could affect the interactions of adsorptive and adsorbent. Such effects are not accounted for in

Table 2 BET area, pore volume calculated by DFT calculations ( $V_{DFT}$ ) and pore volume calculated using a Monte-Carlo method ( $V_{MC}$ ) for low O<sub>2</sub>-flow, high O<sub>2</sub>-flow and the pristine fibres obtained from gas adsorption isotherms of Ar and CO<sub>2</sub>

Sample	BET (m <sup>2</sup> g <sup>-1</sup> )	$V_{DFT(tot)}$ (cm <sup>3</sup> g <sup>-1</sup> )	$V_{DFT<2nm}$ (cm <sup>3</sup> g <sup>-1</sup> )	$V_{DFT<1.5nm}$ (cm <sup>3</sup> g <sup>-1</sup> )	$V_{MC(tot)}$ (cm <sup>3</sup> g <sup>-1</sup> )	$V_{DFT<0.7nm}$ (cm <sup>3</sup> g <sup>-1</sup> )	$V_{MC<0.7nm}$ (cm <sup>3</sup> g <sup>-1</sup> )
Low O <sub>2</sub> -flow	2029	0.831	0.806	0.696	0.605	0.173	0.208
High O <sub>2</sub> -flow	1094	0.461	0.424	0.365	0.446	0.058	0.145
Pristine fibres	13.4	0.016	0.004	0.003	0.180	—	0.101



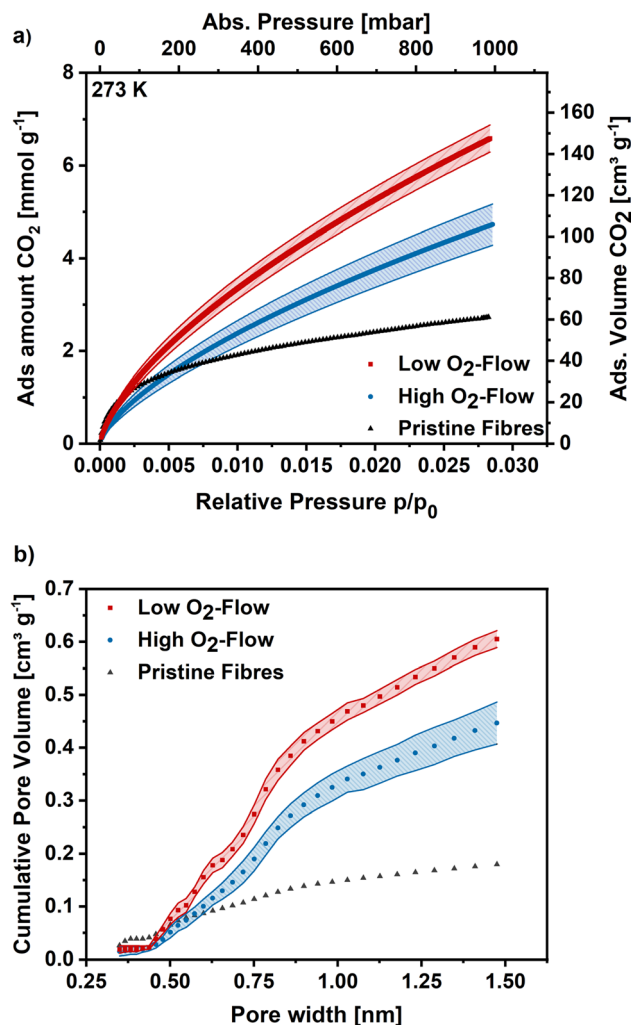


Fig. 8 (a) CO<sub>2</sub> adsorption isotherms at 273 K for high O<sub>2</sub>-flow, low O<sub>2</sub>-flow and the pristine fibres. (b) Determined pore size distribution via Monte-Carlo calculations for pores smaller 1.5 nm.

the standard calculation models used for the determination of the pore size distributions.

Furthermore, the isosteric enthalpy of adsorption was calculated for high and low O<sub>2</sub>-flow based on CO<sub>2</sub> adsorption isotherms measured at 273 K, 283 K and 293 K (S7).<sup>†</sup> For low O<sub>2</sub>-flow a value of 28.9 kJ mol<sup>-1</sup> was determined at a loading of 0.1 mmol g<sup>-1</sup> which slightly decreases to 27.1 kJ mol<sup>-1</sup> at a loading of 6.5 mmol g<sup>-1</sup> (Fig. 9). For high O<sub>2</sub>-flow, the obtained enthalpy of adsorption is at 27.4 kJ mol<sup>-1</sup> at a loading of 0.1 mmol g<sup>-1</sup> and decreases to 23.0 kJ mol<sup>-1</sup> at a loading of 5 mmol g<sup>-1</sup>. Both isosteric enthalpies of adsorption are comparable to adsorption enthalpies of activated electrospun carbon nanofibres in literature.<sup>57</sup> The more distinctive decrease of the isosteric enthalpy of adsorption for high O<sub>2</sub>-flow can be linked to a higher degree of surface oxygen due to the partial carbon oxidation at high O<sub>2</sub>-flow (Table 1), which probably lowers the binding affinity towards CO<sub>2</sub> due to the increased number of acidic groups on the surface.

To get an insight into the adsorption kinetics, equilibration curves of CO<sub>2</sub> at 50 mbar and 298 K were measured (Fig. 9b). For

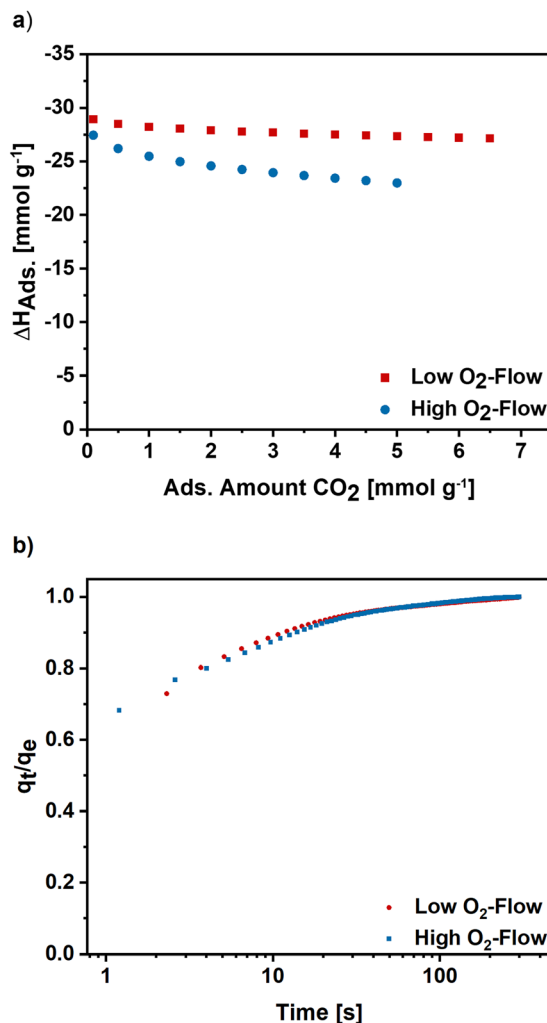


Fig. 9 (a) Isosteric enthalpy of adsorption for high and low O<sub>2</sub>-flow calculated for CO<sub>2</sub> isotherms measured at 273 K, 283 K and 293 K. (b) Normalized adsorption kinetics for high and low O<sub>2</sub>-flow determined at 50 mbar and 298 K.

high and low O<sub>2</sub>-flow the adsorption rate is fast, as the equilibrium loading is reached within the first 100 s with the steepest increase in the first 20 s. Comparing the two post-treatments, there are no significant changes of the adsorption kinetics. Therefore, the choice of post-treatment does not notably affect the adsorption rate of the carbon nanofibres.

Overall, the low O<sub>2</sub>-flow conditions result in improved gas adsorption properties, namely a higher adsorption capacity and a higher micropore volume. Furthermore, the isosteric enthalpy of adsorption is increased for low O<sub>2</sub>-flow, whereas the adsorption kinetics are very similar for both post-treatments. Based on the results, the importance the choice of post-treatment conditions after KOH activation of electrospun carbon nanofibres becomes evident.

## 4. Conclusion

The effect of two atmospheric post-treatments after the KOH activation of electrospun PAN-based carbon nanofibres was



detailed studied with a focus on the occurring pyrophoric effect, chemical reactions during the post-treatment and changes of the morphology and adsorption properties.

At high O<sub>2</sub>-flow conditions a significant formation of heat was observed and related to the oxidation reactions of metallic potassium, which was formed during the activation process prior to the post-treatment step. The reaction heat of the potassium oxidation reactions acts as igniter for a subsequent carbon combustion, which significantly changes the pore structure and surface chemistry of the material and destroys the original fibre structure. The comparability of high O<sub>2</sub>-flow to a usually applied ambient air post-treatment was shown in an additional experiment in which a significant pyrophoric effect was visible.

Control of the vigorous potassium oxidation reactions was enabled by the application of a low O<sub>2</sub>-flow as post-treatment. The low O<sub>2</sub>-flow limits the oxidation reactions, resulting in a reduced heat formation, which is insufficient to cause a carbon combustion. A significant increase in adsorption capacities and accessible pore volume as well as higher enthalpies of adsorption of CO<sub>2</sub> were found for low O<sub>2</sub>-flow samples.

Summarising, this work clearly shows that vigorous potassium oxidation reactions can occur after the KOH activation of electrospun carbon nanofibres and alter the obtained material. By proper choice of the atmospheric post-treatment conditions this potassium oxidation reactions can be limited and a significant improvement of the obtained porosity and surface chemistry can be achieved.

## Data availability

Data will be made available upon reasonable request.

## Conflicts of interest

The authors have no competing interest to declare.

## Acknowledgements

The authors acknowledge funding provided by the Deutsche Forschungsgemeinschaft (DFG, German Research Foundation) under Germany's Excellence Strategy-Cluster of Excellence 2186 'The Fuel Science Center' ID:390919832. The authors thank the Central Institute for Engineering, Electronics and Analytics (ZEA-3) of Forschungszentrum Jülich GmbH for performing CHN analysis and ICP-OES measurements.

## References

- 1 J. Wang and S. Kaskel, KOH activation of carbon-based materials for energy storage, *J. Mater. Chem.*, 2012, **22**, 23710–23725, DOI: [10.1039/C2JM34066F](#).
- 2 N. A. Rashidi and S. Yusup, An overview of activated carbons utilization for the post-combustion carbon dioxide capture, *J. CO<sub>2</sub> Util.*, 2016, **13**, 1–16, DOI: [10.1016/j.jcou.2015.11.002](#).
- 3 X.-Q. Zhang, W.-C. Li and A.-H. Lu, Designed porous carbon materials for efficient CO<sub>2</sub> adsorption and separation, *New Carbon Mater.*, 2015, **30**(6), 481–501, DOI: [10.1016/s1872-5805\(15\)60203-7](#).
- 4 M. Mohan, V. K. Sharma, E. A. Kumar and V. Gayathri, Hydrogen storage in carbon materials—A review, *Energy Storage*, 2019, **1**(2), 1–26, DOI: [10.1002/est2.35](#).
- 5 A. Sharma, J. Jindal, A. Mittal, K. Kumari, S. Maken and N. Kumar, Carbon materials as CO<sub>2</sub> adsorbents: a review, *Environ. Chem. Lett.*, 2021, **19**(2), 875–910, DOI: [10.1007/s10311-020-01153-z](#).
- 6 X.-Y. Li, Y. Yan, B. Zhang, T.-J. Bai, Z.-Z. Wang and T.-S. He, PAN-derived electrospun nanofibers for supercapacitor applications: ongoing approaches and challenges, *J. Mater. Sci.*, 2021, **56**(18), 10745–10781, DOI: [10.1007/s10853-021-05939-6](#).
- 7 U. Kamran, J. R. Choi and S. J. Park, A role of activators for efficient CO<sub>2</sub> affinity on polyacrylonitrile-based porous carbon materials, *Front. Chem.*, 2020, **8**, 1–18, DOI: [10.3389/fchem.2020.00710](#).
- 8 M. Wu, Q. Zha, J. Qiu, Y. Guo, H. Shang and A. Yuan, Preparation and characterization of porous carbons from PAN-based preoxidized cloth by KOH activation, *Carbon*, 2004, **42**(1), 205–210, DOI: [10.1016/j.carbon.2003.10.025](#).
- 9 W. Shen, S. Zhang, Y. He, J. Li and W. Fan, Hierarchical porous polyacrylonitrile-based activated carbon fibers for CO<sub>2</sub> capture, *J. Mater. Chem.*, 2011, **21**(36), 14036–14040, DOI: [10.1039/c1jm12585k](#).
- 10 J. Zhou, X. Wang and W. Xing, Carbon-based CO<sub>2</sub> adsorbents, in *Post-Combustion Carbon Dioxide Capture Materials*, ed. Q. Wang, The Royal Society of Chemistry, 2019, pp. 1–75, DOI: [10.1039/9781788013352-00001](#).
- 11 K. Kaneko and F. Rodriguez-Reinoso, *Nanoporous Materials for Gas Storage*, Springer, 2019, pp. 91–107, DOI: [10.1007/978-981-13-3504-4](#).
- 12 H. Marsh and F. Rodriguez-Reinoso, *Activated Carbon*, Elsevier, 2006, pp. 322–365, DOI: [10.1016/B978-0-08-044463-5.X5013-4](#).
- 13 A. N. Wennerberg and T. M. O'Grady, Active Carbon Process and Composition, *US Pat.* 4082694, 1978.
- 14 N. E. Williams, O. A. Oba and N. P. Aydinlik, Modification, production, and methods of KOH-activated carbon, *ChemBioEng Rev.*, 2022, **9**(2), 164–189, DOI: [10.1002/cben.202100030](#).
- 15 T. Otowa, R. Tanibata and M. Itoh, Production and adsorption characteristics of MAXSORB: high surface-area active carbon, *Gas Sep. Purif.*, 1993, **7**, 241–245.
- 16 T. Otowa, Activation mechanism, surface properties and adsorption characteristics of KOH activated high surface area carbon, *Fundam. Adsorpt.*, 1996, 709–716, DOI: [10.1007/978-1-4613-1375-5\\_88](#).
- 17 E. Raymundo-Piñero, P. Azaïs, T. Cacciaguerra, D. Cazorla-Amorós, A. Linares-Solano and F. Béguin, KOH and NaOH activation mechanisms of multiwalled carbon nanotubes with different structural organisation, *Carbon*, 2005, **43**(4), 786–795, DOI: [10.1016/j.carbon.2004.11.005](#).



- 18 D. Lozano-Castelló, J. M. Calo, D. Cazorla-Amorós and A. Linares-Solano, Carbon activation with KOH as explored by temperature programmed techniques, and the effects of hydrogen, *Carbon*, 2007, **45**(13), 2529–2536, DOI: [10.1016/j.carbon.2007.08.021](#).
- 19 M. Lillo-Ródenas, D. Cazorla-Amorós and A. Linares-Solano, Understanding chemical reactions between carbons and NaOH and KOH, *Carbon*, 2003, **41**, 267–275, DOI: [10.1016/S0008-6223\(02\)00279-8](#).
- 20 B. Petrovic, M. Gorbounov and S. Masoudi Soltani, Influence of surface modification on selective CO<sub>2</sub> adsorption: a technical review on mechanisms and methods, *Microporous Mesoporous Mater.*, 2021, **312**, 1–41, DOI: [10.1016/j.micromeso.2020.110751](#).
- 21 D. Lozano-Castelló, M. A. Lillo-Ródenas, D. Cazorla-Amorós and A. Linares-Solano, Carbon activation by alkaline hydroxides, in *Chem. Phys. Carbon*, ed. L. R. Radovic, CRC Press Taylor and Francis Group, 2008, pp. 1–56, DOI: [10.1201/9781420042993](#).
- 22 N.-G. Vannerberg, Peroxides, Superoxides, and Ozonides of the Metals of Groups Ia IIa and IIb, *Prog. Inorg. Chem.*, 1962, **4**, 125–297, DOI: [10.1002/9780470166055.ch3](#).
- 23 I. I. Vol'nov, *Peroxides, Superoxides, and Ozonides of Alkali and Alkaline Earth Metals*, Springer, New York, 1966, pp. 21–120.
- 24 K. Fredenhagen and G. Cadenbach, Die Bindung von Kalium dutch Kohlenstoff, *Z. Anorg. Allg. Chem.*, 1926, **158**(1), 249–263, DOI: [10.1002/zaac.19261580122](#).
- 25 H. Marsh, N. Murdie, I. A. S. Edwards and H. P. Boehm, *Chemistry and Physics of Carbon*, Marcel Dekker Inc., ed. P. A. Thrower, 1987, vol. 20, pp. 213–268, DOI: [10.1201/9781003209034](#).
- 26 F. Kapteijn, J. Jurriaans and J. A. Moulijn, Formation of intercalate-like structures by heat treatment of K<sub>2</sub>CO<sub>3</sub>-carbon in an inert atmosphere, *Fuel*, 1983, **62**, 249–251, DOI: [10.1016/0016-2361\(83\)90210-7](#).
- 27 C. Herinckx, R. Perret and W. Ruland, Interstitial Compounds of Potassium with Carbon Fibres, *Nature Volume*, 1968, **220**, 63–64.
- 28 W. Rüdorff, E. Schulze and Z. Anorg, Über Alkaligraphitverbindungen, *Allg. Chem.*, 1954, **277**(3–4), 156–171, DOI: [10.1002/zaac.19542770307](#).
- 29 V. Selmert, A. Kretzschmar, H. Weinrich, H. Kungl, H. Tempel and R. A. Eichel, CO<sub>2</sub>/N<sub>2</sub> separation on highly selective carbon nanofibers investigated by dynamic gas adsorption, *ChemSusChem*, 2022, **15**, 1–12, DOI: [10.1002/cssc.202200761](#).
- 30 A. Kretzschmar, V. Selmert, H. Weinrich, H. Kungl, H. Tempel and R. A. Eichel, Tailored gas adsorption properties of electrospun carbon nanofibers for gas separation and storage, *ChemSusChem*, 2020, **13**(12), 3180–3191, DOI: [10.1002/cssc.202000520](#).
- 31 R. Schierholz, D. Kröger, H. Weinrich, M. Gehring, H. Tempel, H. Kungl, J. Mayer and R.-A. Eichel, The carbonization of polyacrylonitrile-derived electrospun carbon nanofibers studied by *in situ* transmission electron microscopy, *RSC Adv.*, 2019, **9**(11), 6267–6277, DOI: [10.1039/c8ra10491c](#).
- 32 A. Kretzschmar, V. Selmert, H. Kungl, H. Tempel and R. A. Eichel, Application of a tailorable carbon molecular sieve to evaluate concepts for the molecular dimensions of gases, *Microporous Mesoporous Mater.*, 2022, **343**, 1–9, DOI: [10.1016/j.micromeso.2022.112156](#).
- 33 J. Park, A. Kretzschmar, V. Selmert, O. Camara, H. Kungl, H. Tempel, S. Basak and R. A. Eichel, Structural study of polyacrylonitrile-based carbon nanofibers for understanding gas adsorption, *ACS Appl. Mater. Interfaces*, 2021, **13**(39), 46665–46670, DOI: [10.1021/acsami.1c13541](#).
- 34 J. Borowec, V. Selmert, A. Kretzschmar, K. Fries, R. Schierholz, H. Kungl, R. A. Eichel, H. Tempel and F. Hausen, Carbonization-temperature-dependent electrical properties of carbon nanofibers-from nanoscale to macroscale, *Adv. Mater.*, 2023, **35**(31), e2300936, DOI: [10.1002/adma.202300936](#).
- 35 G. Hotová and V. Slovák, Quantitative TG-MS analysis of evolved gases during the thermal decomposition of carbon containing solids, *Thermochim. Acta*, 2016, **632**, 23–28, DOI: [10.1016/j.tca.2016.03.012](#).
- 36 J. Tóth, Uniform interpretation of gas/solid adsorption, *Adv. Colloid Interface Sci.*, 1995, **55**, 1–239, DOI: [10.1016/0001-8686\(94\)00226-3](#).
- 37 J. L. Rouquerol and P. F. Rouquerol, Is the BET equation applicable to microporous adsorbents?, *Stud. Surface Sci. Catalysis*, 2007, **160**, 49–56, DOI: [10.1016/S0167-2991\(07\)80008-5](#).
- 38 M. Thommes, K. Kaneko, A. V. Neimark, J. P. Olivier, F. Rodriguez-Reinoso, J. Rouquerol and K. S. W. Sing, Physisorption of gases, with special reference to the evaluation of surface area and pore size distribution (IUPAC Technical Report), *Pure Appl. Chem.*, 2015, **87**(9–10), 1051–1069, DOI: [10.1515/pac-2014-1117](#).
- 39 A. Nuhnen and C. Janiak, A practical guide to calculate the isosteric heat/enthalpy of adsorption *via* adsorption isotherms in metal-organic frameworks, MOFs, *Dalton Trans.*, 2020, **49**(30), 10295–10307, DOI: [10.1039/d0dt01784a](#).
- 40 M. W. J. Chase, NIST-JANAF thermochemical tables, *J. Phys. Chem. Ref. Data*, 1998, 1465–1489.
- 41 R. Bovard, Oxygen sources for space flights, *Aerosp. Med.*, 1960, 407–412.
- 42 C. B. Jackson and R. C. Werner, Manufacture and use of potassium superoxide, in *Handling and Uses of the Alkali Metals*, American Chemical Society, 1957, pp. 174–177, DOI: [10.1021/ba-1957-0019.ch019](#).
- 43 J. Singh, H. Bhunia and S. Basu, Adsorption of CO<sub>2</sub> on KOH activated carbon adsorbents: effect of different mass ratios, *J. Environ. Manage.*, 2019, **250**, 1–9, DOI: [10.1016/j.jenvman.2019.109457](#).
- 44 Y. K. Kim, G. M. Kim and J. W. Lee, Highly porous N-doped carbons impregnated with sodium for efficient CO<sub>2</sub> capture, *J. Mater. Chem. A*, 2015, **3**(20), 10919–10927, DOI: [10.1039/c5ta01776a](#).
- 45 J. S. Im, S. J. Park, T. J. Kim, Y. H. Kim and Y. S. Lee, The study of controlling pore size on electrospun carbon





- nanofibers for hydrogen adsorption, *J. Colloid Interface Sci.*, 2008, **318**(1), 42–49, DOI: [10.1016/j.jcis.2007.10.024](https://doi.org/10.1016/j.jcis.2007.10.024).
- 46 S.-H. Yoon, S. Lim, Y. Song, Y. Ota, W. Qiao, A. Tanaka and I. Mochida, KOH activation of carbon nanofibers, *Carbon*, 2004, **42**(8–9), 1723–1729, DOI: [10.1016/j.carbon.2004.03.006](https://doi.org/10.1016/j.carbon.2004.03.006).
- 47 J. Wang, Y. K. Park and Y. M. Jo, Sequential improvement of activated carbon fiber properties for enhanced removal efficiency of indoor CO<sub>2</sub>, *J. Ind. Eng. Chem.*, 2020, **89**, 400–408, DOI: [10.1016/j.jiec.2020.06.011](https://doi.org/10.1016/j.jiec.2020.06.011).
- 48 J. Romanos, M. Beckner, T. Rash, L. Firlej, B. Kuchta, P. Yu, G. Suppes, C. Wexler and P. Pfeifer, Nanospace engineering of KOH activated carbon, *Nanotechnology*, 2012, **23**(1), 1–7, DOI: [10.1088/0957-4484/23/1/015401](https://doi.org/10.1088/0957-4484/23/1/015401).
- 49 A.-N. A. El-Hendawy, An insight into the KOH activation mechanism through the production of microporous activated carbon for the removal of Pb<sup>2+</sup> cations, *Appl. Surf. Sci.*, 2009, **255**(6), 3723–3730, DOI: [10.1016/j.apsusc.2008.10.034](https://doi.org/10.1016/j.apsusc.2008.10.034).
- 50 J. Wang, A. Heerwig, M. R. Lohe, M. Oschatz, L. Borchardt and S. Kaskel, Fungi-based porous carbons for CO<sub>2</sub> adsorption and separation, *J. Mater. Chem.*, 2012, **22**(28), 13911–13913, DOI: [10.1039/c2jm32139d](https://doi.org/10.1039/c2jm32139d).
- 51 D. Lozano-Castelló, M. A. Lillo-Ródenas, D. Cazorla-Amorós and A. Linares-Solano, Preparation of activated carbons from Spanish anthracite. Activation by KOH, *Carbon*, 2000, **39**, 741–749, DOI: [10.1016/S0008-6223\(00\)00185-8](https://doi.org/10.1016/S0008-6223(00)00185-8).
- 52 N. Yoshizawa, K. Maruyama, Y. Yamada, E. K. M. Ishikawa, Y. Toda and M. Shiraishi, XRD evaluation of KOH activation process and influence coal rank, *Fuel*, 2002, **81**, 1717–1722, DOI: [10.1016/S0016-2361\(02\)00101-1](https://doi.org/10.1016/S0016-2361(02)00101-1).
- 53 Y.-C. Chiang, C.-Y. Yeh and C.-H. Weng, Carbon dioxide adsorption on porous and functionalized activated carbon fibers, *Appl. Sci.*, 2019, **9**(10), 1–15, DOI: [10.3390/app9101977](https://doi.org/10.3390/app9101977).
- 54 J. Singh, H. Bhunia and S. Basu, Adsorption of CO<sub>2</sub> on KOH activated carbon adsorbents: effect of different mass ratios, *J. Environ. Manage.*, 2019, **250**, DOI: [10.1016/j.jenvman.2019.109457](https://doi.org/10.1016/j.jenvman.2019.109457).
- 55 G. Zainab, A. A. Babar, N. Ali, A. A. Aboalhassan, X. Wang, J. Yu and B. Ding, Electrospun carbon nanofibers with multi-aperture/opening porous hierarchical structure for efficient CO(2) adsorption, *J. Colloid Interface Sci.*, 2020, **561**, 659–667, DOI: [10.1016/j.jcis.2019.11.041](https://doi.org/10.1016/j.jcis.2019.11.041).
- 56 Y.-C. Chiang, C.-C. Huang and W.-T. Chin, Carbon dioxide adsorption on carbon nanofibers with different porous structures, *Appl. Sci.*, 2021, **11**(16), 7724, DOI: [10.3390/app11167724](https://doi.org/10.3390/app11167724).
- 57 Y. C. Chiang, W. T. Chin and C. C. Huang, The application of hollow carbon nanofibers prepared by electrospinning to carbon dioxide capture, *Polymers*, 2021, **13**(19), 3275, DOI: [10.3390/polym13193275](https://doi.org/10.3390/polym13193275).

